Enhanced risk of concurrent regional droughts with increased ENSO variability and warming

Jitendra Singh[1], Moetasim Ashfaq[2], Christopher B. Skinner[3], Weston B. Anderson[4], Vimal Mishra[5,6] and Deepti Singh[1]

[1]School of the Environment, Washington State University, Vancouver, WA, USA.
[2]Computational Sciences and Engineering Division, Oak Ridge National Laboratory, Oak Ridge, TN, USA.
[3]Department of Environmental, Earth and Atmospheric Sciences, University of Massachusetts Lowell, Lowell, MA, USA.
[4]International Research Institute for Climate and Society, Columbia University, Palisades, NY, USA.
[5]Civil Engineering, Indian Institute of Technology (IIT) Gandhinagar, Gandhinagar, India. [6]Earth Sciences, Indian Institute of Technology (IIT) Gandhinagar, Gandhinagar, India.

Abstract:

Spatially compounding extremes pose substantial threats to globally interconnected socio-economic systems. Here we use multiple large ensemble simulations of the high-emissions scenario to show increased risk of compound droughts during the boreal summer over ten global regions. Relative to the late twentieth century, the probability of compound droughts increases by ~40% and ~60% by the middle and late twenty-first century, respectively, with a disproportionate increase in risk across North America and the Amazon. These changes contribute to an approximately ninefold increase in agricultural area and population exposure to severe compound droughts with continued fossil-fuel dependence. ENSO is the predominant large-scale driver of compound droughts with 68% of historical events occurring during El Niño or La Niña conditions. With ENSO tele- connections remaining largely stationary in the future, a ~22% increase in frequency of ENSO events combined with projected warming drives the elevated risk of compound droughts.

Acknowledgement

We would like to thank the National Center for Atmospheric Research (NCAR), Climate Hazards Center UC Santa Barbara and US CLIVAR Working Group on Large Ensembles for archiving and enabling public access to their data. We thank Washington State University for the startup funding that has supported J.S. and D.S. W.B.A. acknowledges funding from Earth Institute Postdoctoral Fellowship. M.A. was supported by the US Air Force Numerical Weather Modeling Program and the National Climate-Computing Research Center, which is located within the National Center for Computational Sciences at the ORNL and supported under a Strategic Partnership Project (no. 2316-T849-08) between DOE and NOAA. This manuscript has been co-authored by employees of Oak Ridge National Laboratory, managed by UT Battelle, LLC, under contract no. DE-AC05- 00OR22725 with the US Department of Energy (DOE). The publisher, by accepting the article for publication, acknowledges that the US Government retains a non-exclusive, paid-up, irrevocable, world-wide license to publish or reproduce the published form of this manuscript, or allow others to do so, for US Government purposes. The US DOE will provide public access to these results of federally sponsored research in accordance with the DOE Public Access Plan (http://energy.gov/downloads/doe-public-access-plan).

Spatially and/or temporally compounding Earth system extremes can lead to cascading impacts on global socio-economic systems[1–5]. Several recent studies have examined temporally compounding events that result from different combinations of climatic hazards occurring in the same location at the same time, such as hot and dry conditions[6,7], or heavy precipitation and extreme winds[8]. The simultaneous occurrence of extremes across multiple regions—referred to as spatially compound extremes—have received relatively limited attention. Spatially com- pound extremes have the potential to accumulate hazard impacts in distant locations and pose amplifying pressures on a network of interconnected socio-economic systems[1,9–14]. For example, severe droughts that concurrently occurred across Asia, Brazil and Africa during 1876 to 1878 led to synchronous crop failures, followed by famines that killed more than 50 million people in those regions[15]. The complex and interconnected nature of the current global food network generates agricultural shocks—even over a few individual regions—capable of having ripple effects on global food prices and food security, particularly in socioeconomically vulnerable regions[10,16]. Compound extremes can also influence global economies through their impacts on international agribusiness and reinsurance industries[6,17,18]. Understanding the drivers of simultaneous extremes across regions and the exposure of human systems to such extremes can thus inform assessments of the climate risks to inter- connected systems and planning for their societal impacts.

Recent studies have examined the risk of crop failures from com- pound extremes and highlighted various physical drivers and mechanisms. The risk of multiple breadbasket failures is elevated during the simultaneous physical hazards imposed by the large-scale natural climate variability modes such as El Niño–Southern Oscillation (ENSO), Indian Ocean Dipole and Atlantic Niño[11,12,19]. ENSO is one of the predominant drivers of hydroclimate variability across tropical regions and El Niño events are associated with several major historical synchronous droughts and extreme temperatures across Asia, Africa and South America[6,15,20,21]. For instance, the strong El Niño event in 1983 caused extreme heatwaves and droughts across multiple maize-producing regions that resulted in the most extensive simultaneous crop failures in recent records[12,16]. Projected anthropogenic warming is expected to double the risk of concurrent hot and dry extremes over certain croplands and pastures[6], and enhance the risk of globally synchronized shocks on temperature-sensitive crops such as Maize[14], highlighting the importance of understanding such drivers of compounding stressors.

A recent study used observations and unforced climate simulations to examine the influence of multiple natural variability modes on spatially compound droughts (hereafter compound droughts) during the boreal summer season and found El Niño to be the dominant driver of widespread and severe compound droughts[19]. Nearly 80% of observed compound droughts across the tropical/subtropical belt between 1901–2018 were associated with El Niño events[19]. Here we aim to: (1) quantify changes in concurrent drought characteristics between the present day and the mid- and late twenty-first century; (2) understand the role of projected changes in ENSO characteristics on projected concurrent droughts; and (3) characterize the changing risks from such simultaneous climate shocks to agriculture and people. We primarily use the 40-member Community Earth System Model version 1 (CESM1) large ensemble simulations (LENS) for the high-emissions representative concentration path- way 8.5 (RCP8.5), but incorporate other large ensemble simulations from the single-model initial-condition large ensemble (SMILE) archive to assess uncertainties in the projected changes and their drivers. We prioritize using single-model large ensembles over multimodel ensembles with limited ensemble sizes to comprehensively assess the role of natural variability modes as an important driver of extremes under different climate regimes and characterize irreducible uncertainty in projected changes.

Our analysis focuses on ten tropical and subtropical regions defined in the IPCC *Special Report on Managing the Risks of Extreme Events and Disasters to Advance Climate Change Adaptation* (SREX)[22], which receive a large fraction of their annual precipitation during the summer season and experience substantial sub- seasonal precipitation variability (Methods and Extended Data Fig. 1). Several of these regions exhibit similar socio-economic and climate characteristics (Extended Data Fig. 1a–d), including areas in which rainy seasons and agricultural production are strongly influenced by the global monsoon systems. These regions also include important breadbaskets and vulnerable populations that depend on rainfed agriculture for their livelihood[23,24]. Given the importance of ENSO for hydroclimate variability over many of these regions[12,15,25–28] (Extended Data Fig. 1c), we investigate the influence of El Niño and La Niña events on compound drought characteristics in the historical and late twenty-first century climate. We also quantify future changes in the exposure of population and agricultural compound droughts to evaluate the societal implications of projected changes.

Historical and Future Characteristics of Compound Droughts

To account for the influence of temperature and vegetation responses to elevated CO_2 concentrations, we define droughts on the basis of the multivariate standardized precipitation evapotranspiration index (SPEI) calculated from precipitation and evapotranspiration (see Methods). Using the CESM1 LENS, we find statistically significant (P-value < 0.05) increases in the frequency, spatial extent and average intensity of compound droughts in the mid (2031–2060) and late twenty-first century (2071–2100) under the RCP8.5 trajectory relative to the late twentieth century (1971–2000) (Fig. 1). The number of regions concurrently experiencing drought increases significantly (P-value < 0.05) with warming (Fig. 1a), contributing to an increase in the probability of compound droughts (≥3 regions simultaneously under drought) by ~40% in the mid-twenty-first century and ~60% in the late twenty-first century relative to historical (historical probability = 0.32 and future probabilities = 0.45 and 0.51). Applying a bootstrap test, we find that the projected changes in the probability of compound droughts are not solely driven by changes in drought occurrence over a single region but are representative of increasing drought risk across multiple regions with warming (Supplementary Fig. 1), consistent with other twenty-first century drought projections[29].

The fraction of drought-affected area during compound droughts also significantly (P-value < 0.05) increases with warming, with the probability of widespread compound droughts (events with drought-affected areas exceeding the historical 90th percentile; see Methods) increasing by ~20% in the mid twenty-first century and ~30% in the late twenty-first century (Fig. 1b). Furthermore, the average severity of compound droughts also increases in both future periods (Fig. 1c). These changes result in an approximately threefold (probability = 0.27) and greater than sevenfold (probability = 0.76) increase in the probability of severe compound droughts (events with intensity more severe than the historical tenth per- centile; see Methods) during the mid and late twenty-first century, respectively, relative to historical climate (probability = 0.1). As of four compound droughts in the late first century are classified as severe (Fig. 1c).

Increasing Exposure to Compound Droughts

We quantify the impacts of more frequent, widespread and severe compound droughts on agricultural areas (the combination of cropland and pastureland) and population by calculating changes in their exposures to compound droughts in the late twenty-first century relative to the late

twentieth century on the basis of CESM1 LENS (Fig. 2). In the late twenty-first century, agricultural area expo- sure to severe compound droughts—estimated as the simultaneous agricultural land exposed multiplied by the probability of severe compound droughts—increases by around tenfold compared with the late twentieth century. An average of ~0.7 million km^2 (~5% of total agricultural area across the ten regions) and ~0.3 million km^2 (~1.5%) of agricultural area per year is at risk of being simultaneously exposed to severe compound droughts during 2071–2100 and 2031–2060, respectively, compared with ~0.065 million km^2 per year (~0.5%) in the 1971–2000 period (Fig. 2a). By contrast, although agricultural exposure to moderate compound droughts increases slightly during 2031–2060, it decreases to half by the late twenty-first century as more future compound droughts are severe rather than moderate (Extended Data Fig. 2). As the agricultural area does not change in the two analyses periods, the difference in exposure is mainly driven by changes in the frequencies and extent of moderate and severe compound droughts as well as the regions they affect in the two climates.

An increase in the severity of compound droughts in the late twenty-first century is associated with changes in the characteristics of the water cycle. Specifically, several regions either exhibit a decrease in precipitation (CNA, CAM and northern AMZ) (Extended Data Fig. 3a,b) or an increase in evapotranspiration (TIB, ENA and northern CAM), both of which enhance drying (Extended Data Fig. 3c,d) and elevate the risk of droughts relative to other regions (Fig. 2c), consistent with Cook et al.29. Consequently, whereas exposure of agricultural areas aggregated across all regions to severe compound drought increases due to the higher prob- ability of severe compound droughts in the future, the future risk is greatest over AMZ (approximately tenfold increase in exposure) and CAM, CAN and TIB (~15-fold increase in exposure) (Fig. 2c,d and Extended Data Fig. 4). By contrast, future summer precipitation increases more than evapotranspiration over EAS, SAS, SEA, WAF and EAF, and therefore these regions are less likely to experience compound droughts in the future and have relatively smaller increases in agricultural exposure (Fig. 2c,d). Although we find a reduction in drought likelihood is projected over EAF, a region with high historical drought risk, we note that there is considerable uncertainty in the response of EAF precipitation to warming[30].

Increases in the frequency and severity of compound droughts also contributes to increases in population exposure to severe com- pound droughts (Fig. 2b). Population exposure to projected changes in severe compound droughts—defined as the simultaneous population exposed multiplied by the probability of an event—increases by around fourfold and ninefold under population projections from the Shared Socioeconomic Pathways 5 (SSP5) in the mid and late twenty-first century, respectively, whereas exposure to moderate compound droughts declines half during the late twenty-first century (Fig. 2a and Extended Data Fig. 2). In the historical climate, an average of ~13 million people are at risk of experiencing severe compound droughts every year, which increases to an average of ~120 million people every year by the late twenty-first century (Fig. 2b). This large increase in population exposure to severe compound droughts is driven by projected increases in the frequency of severe compound droughts and in population over EAF, WAF, ENA, CNA, SAS and parts of SEA[31] (Fig. 2e) under SSP5 despite decreases in the likelihood of EAF, WAF and SAS being affected by compound droughts (Fig. 2c).

Physical drivers of compound droughts

The projected changes in compound drought characteristics are associated with changes in ENSO characteristics in addition to warming. Historically, ~68% of compound droughts are associated with ENSO events, of which El Niño conditions alone account for ~46% (Fig. 3). In the late twenty-first century, the fraction of com- pound droughts associated with ENSO events increases to ~75% and approximately half of them are associated with El Niño conditions (Fig. 3b). With projected warming, the number of ENSO events increases from 712 events during 1971–2000 to 869 events during 2071–2100 in the 40-member CESM ensemble (Fig. 3a,b). An increase in extreme ENSO events is consistent with previous studies with multiple models[32,33]. Overall, this ~22% increase in El Niño and La Niña events contributes to a ~70% increase in the total number of compound droughts associated with El Niño and La Niña events between the late twentieth (263 events) and late twenty-first centuries (448 events). This disproportionate increase in compound droughts could be a consequence of warming-driven increases in droughts in several regions and intensified land–atmosphere feedbacks[34,35]. We also find that the number of compound droughts associated with non-ENSO drivers exhibit a moderate increase of ~25% (Fig. 3b). Collectively, these results indicate that ENSO events are a major driver of compound droughts in both climates and their more frequent occurrence contributes to more compound droughts in a warmer climate.

The more prominent role of El Niño compared with La Niña in driving spatially compound droughts in historical and future climates is due to the negative correlation of ENSO with precipitation variability over most of the study regions (Fig. 4). El Niño-related compound droughts have a different spatial pat- tern across these regions relative to La Niña-related compound droughts. El Niño conditions lead to intense and widespread drying over CAM, AMZ, WAF, EAF, EAS, southern SAS and SEA in the historical climate (Fig. 4a,b). Among the ten regions, AMZ, CAM, EAF and SEA show the highest likelihood of being part of compound droughts during El Niño conditions in the historical climate (Fig. 4e). This likelihood increases across AMZ, CAM and CNA, and decreases over SEA, SAS, EAS, EAF and WAF in the late twenty-first century[36–39]. By contrast, La Niña conditions lead to drier conditions over relatively fewer regions, including CNA, ENA, southern WAF, Eastern SAS and northern SEA[40] (Fig. 4c,d). The CNA, ENA and SAS regions show the highest likelihood of being part of compound droughts during La Niña conditions in the historical climate (Fig. 4e). This likelihood increases substantially across ENA, CNA and CAM, and decreases over SAS and EAS in the late twenty-first century. Overall, these regional changes in the drought likelihood are consistent with the previous studies highlighting the eastern–western hemispheric asymmetry in the precipitation response to warming. Monsoon precipitation over the Americas is expected to decline due to projected eastern Pacific warming[36–38], whereas, Asian–northern African monsoon precipitation is expected to increase with warming because of enhanced moisture supply over these regions[37–39].

Due to differences in their regional influences, El Niños are associated with a significantly (P-value < 0.05 based on two sam- pled chi-square test) higher number of regions simultaneously (median ≈ four regions) under drought compared with La Niña and non-ENSO drivers (median ≈ three regions) in both climates (Fig. 5a). This contributes to nearly two times as many compound droughts associated with El Niño conditions than La Niña condi- tions. This relatively higher occurrence of compound droughts during El Niño compared with La Niña conditions is not significantly changed by warming (Fig. 3b). Furthermore, El Niño-driven com- pound droughts exhibit significantly (P-value < 0.05) larger mean drought extent (~5%) compared with La Niña-driven compound droughts in both climates and non-ENSO compound droughts in the historical climate (Fig. 5a–c). Although La Niña-driven com- pound droughts exhibit significantly (P-value < 0.05) higher mean intensity in the historical climate, El Niño-driven compound droughts are significantly (P-value < 0.05) more intense in the late twenty-first century relative to La Niña and non-ENSO drivers, largely contributed by stronger dry conditions (~15%) over EAF and WAF (Figs. 4 and 5c). Furthermore, El Niño-driven compound droughts have higher extreme severity than those associated with other drivers as indicated by the higher tails (Fig. 5c). The changes in compound drought characteristics are associated with changes in the regions affected, changes in mean hydroclimate conditions and the strength of associated regional teleconnections (Fig. 4).

ENSO teleconnections

We investigate changes in the influence of ENSO over the study regions by examining its teleconnections with SPEI (Figs. 4 and 6) and precipitation anomalies across the study regions (Supplementary Fig. 2). The magnitude and spatial pattern of correlations

relations between the summer ENSO index and the SPEI (precipitation) are broadly similar in the late twenty-first century and historical climates over most regions with a few exceptions. The area with a significant (P-value < 0.05) correlation between SPEI and ENSO significantly (P-value < 0.05) increases over ENA (from ~40% to ~67%) and decreases over CNA (from ~62% to ~53%) in the future (Fig. 6c). The average correlation significantly (P-value < 0.05) increases from ~0.26 to ~0.34 over WAF and from ~0.35 to ~0.4 over EAF (Fig. 6d). The SPEI spatial composites show stronger dry conditions over western EAF during El Niño conditions and over southern WAF and eastern ENA during La Niña conditions in the future climate (Supplementary Fig. 3). Similarly, wet conditions also exhibit strengthening over southern WAF and eastern ENA during El Niño, and over eastern EAF during La Niña conditions (Supplementary Fig. 3).

Despite these few exceptions, we find that >70% of the area within seven of the ten regions have significant (P-value < 0.05) correlations of a similar sign between ENSO and SPEI during both historical and late twenty-first century climates (Fig. 6e). Fig. 6c–e indicates that ENSO conditions influence a similar area within most regions with similar strength in both climates, which implies that the nature of ENSO teleconnections remains largely stationary with warming. Given the strong role of ENSO events in shaping compound droughts in a warmer climate, these findings highlight the importance of understanding the current ENSO–compound droughts relationship and their related physical processes[19].

Uncertainties in compound droughts and ENSO response

Although our analysis is focused on investigating the drivers of compound droughts and their exposure based on the CESM1 LENS, we use large ensemble simulations with another global climate model—the Canadian Earth System Model version 2 (CanESM2) from the SMILE archive[41]—to evaluate the robustness of our findings to model uncertainties. Our evaluation of uncertain- ties is limited to these two large ensembles due to the unavailability of data from other models (see Methods for model selection criteria). Overall, CanESM2 shows strong consistency with CESM1 in historical compound drought characteristics and their mid and late twenty-first century changes. The CanESM2 large ensemble also shows increases in the probability of compound droughts as well as their extent and severity in the future (Supplementary Fig. 4a–c). The changes in probability of widespread and severe compound droughts in CanESM2 in the late twenty-first century are even higher than those projected for the same period with the CESM1 LENS. Consistent with CESM1, the projected changes in the prob- ability of compound droughts in CanESM2 are not sensitive to changes in drought occurrence over a single region (Supplementary Fig. 1b; see Methods for more details).

Although CESM is one of the most skillful models in reproducing ENSO teleconnections[42] and its projection of increasing frequency of future extreme ENSO conditions is consistent with recent studies that are based on CMIP5[32,33] and CMIP6[43,44] models, we acknowledge that there are still unresolved uncertainties in the response of ENSO events to projected warming[45]. We therefore examine the uncertainties in the ENSO response to historical forcing and future warming using large ensemble simulations from the six SMILE models (including CESM1) and assess the sensitivity of El Niño and La Niña frequency to varying definitions[32,33] (Extended Data Fig. 5 and Supplementary Table 1).

Although CESM shows an increase in the frequency of both extreme El Niño and extreme La Niña events whereas other models show mixed responses of ENSO to future warming (Extended Data Fig. 5 and Supplementary Table 1). In addition to inter-model differences in ENSO event frequency due to background climate state[46] and nonlinearity of sea surface temperature (SST) response[33], we find that the frequency of ENSO events in models is sensitive to the definitions of El Niño and La Niña events (Extended Data Fig. 5 and Supplementary Table 1). For instance, three out of six models show increasing frequencies of El Niño in the future when it is defined on the basis of Niño3 rainfall rates[33,46], whereas only two models show an increase in the projected frequency of El Niño on the basis of Niño3.4 SST (Extended Data Fig. 5 and Supplementary Table 1). Similarly, La Niña's response is also mixed in the climate models and sensitive to the event definition (Supplementary Table 1).

CESM is the only model that shows a consistent future increase in frequency of extreme El Niño and La Niña conditions across various definitions (Supplementary Table 1). By contrast, CanESM2 shows a decrease in the extreme La Niña frequency regardless of metric used but it shows increase in the frequency of extreme El Niño based on precipitation-based metric and decrease based on SST-based metric (Supplementary Table 1). Despite the differences in the frequency of ENSO events, both CESM and CanESM2 models show that the fraction of ENSO events associated with compound droughts is higher in a warmer future relative to historical climate

Discussion

Droughts are associated with a range of environmental, economic and social impacts. Given the increasing global connectivity of socio-economic systems, understanding the historical characteristics of compound droughts and anticipating their changes in a warmer future climate is important for a broad suite of interconnected, climate-sensitive sectors[6]. The agricultural sector, in particular, is highly sensitive to simultaneous shocks across multiple regions due to the complex networks of food supply, demand and global trade[5]. We find a significant (P-value < 0.05) increase in the frequency, extent and intensity of compound droughts in the mid and late twenty-first century relative to the historical late twentieth century climate. The probability of compound droughts (≥3 regions simultaneously under drought) increases by ~40% and ~60% in the mid and late twenty-first century, respectively, relative to the recent historical period under the RCP8.5 scenario. These changes contribute to an around tenfold increase in agricultural exposure to severe compound droughts by the late twenty-first century with continued fossil-fuel dependence, highlighting the higher risk of simultaneous production shocks across a wider extent in more breadbaskets. Increasing exposure of multiple agricultural areas to such simultaneous shocks could increase volatility in global food availability and exacerbate food insecurity.

Our results indicate that the North and South American regions are more likely to experience compound droughts in a future warmer climate as compared to the study regions in Asia and Africa, where much of the areas affected by monsoons are projected to become wetter[39]. The contribution of food produced within the Americas to the global food system could, therefore, be more susceptible to such climatic hazards. For instance, the United States is a major exporter of staple grains and currently exports maize (soyabean) to >160 (>90) countries across the globe[10,47]. Therefore, a modest increase in the risk of compound droughts in the future climate can lead to regional supply shortfalls that could

cascade into the global market, affecting global prices and amplifying food insecurity. Furthermore, our results have broader implications for the global virtual water trade network involved in the water-intensive agricultural, forestry, industrial and mining products[48,49]. In the past three decades, international trade of virtual water has tripled[49] and is expected to increase further in response to increases in population and demand by the end of the twenty-first century[50]. The projected increases in the frequency and severity of compound droughts could therefore disrupt the supply–demand network of such water-intensive goods and thereby, can affect their availability and prices in global market.

In addition to impacts on agriculture and virtual water markets, the interplay of projected growth in population and changes in compound drought characteristics can also exacerbate direct population exposure to drought impacts. Under the low population growth, high fossil-fuel dependent SSP5 trajectory, the population exposure to severe compound droughts increases by approximately ninefold by the late twenty-first century relative to historical. SSP5 represents a future of energy-intensive, fossil fuel-based technological and economic growth along with higher investment in human capital and more integrated global markets[31]. Although the assumed adaptation under this scenario might contribute to a world more resilient to certain climate impacts, the increasing interconnectedness of global markets projected under this scenario might make society more exposed to such compound extremes and consequently causing higher socio-economic impacts. Further, the substantial increase in population exposure can amplify stresses on international agencies responsible for disaster relief by requiring the provision of humanitarian aid to a greater number of people simultaneously exposed to drought-related disasters.

Efforts to better understand and constrain model uncertainties in the response of ENSO to warming and the hydroclimatic impacts of ENSO variability, however, can support predictability and management of compound drought impacts in a warmer climate. Our findings suggest that the regional teleconnections during El Niño or La Niña conditions do not change substantially across most regions except for a significant (P-value < 0.05) increase in the area with ENSO teleconnection over CNA and ENA and strengthening over WAF and EAF. These results imply that when ENSO events occur, they will likely affect the same geographical regions albeit with greater severity. The occurrence of nearly 75% of compound droughts with ENSO events in the future climate highlights the potential for predictability of compound droughts and their impact at lead times of up to 9-months[51]. Timely predictions of compound droughts and their impacts on agricultural areas and communities can facilitate international agribusiness industries to minimize the economic losses and insurance and reinsurance industries to design effective insurance schemes to reduce losses from simultaneous disasters.

We note a few limitations of our study. First, although our analysis is primarily based on CESM1, which is skillful at capturing ENSO characteristics and its teleconnection with precipitation[42], we do not comprehensively account for inter-model differences in reproducing ENSO patterns in assessing projection uncertainties; however, these limitations can be addressed by considering a larger set of Earth System model LENS that will eventually be available through CMIP6 to examine the uncertainties in ENSO responses to future warming. Second, we focus on compound droughts only during the boreal summer season but the influence of ENSO teleconnections on these and other related regions in subsequent seasons has not been considered but could provide additional insights relevant into compounding societal impacts. Future studies can consider potential lead–lag relationships between ENSO and precipitation in spatially and temporally compound extremes analyses. Third, we examine projections under the RCP8.5 trajectory, a high-end fossil-fuel dependent emissions scenario that no longer represents the current emissions trajectory, as we aim to maximize signal to noise to gain physical insights into how warming can affect compound drought characteristics and their physical drivers. The level of forcing and warming represented by this scenario, while still possible especially with strong carbon-cycle feedbacks and high climate sensitivity is a low-likelihood, "worst-case" outcome. Further analyses with additional SSP scenarios are needed to quantify uncertainty in compound droughts and their societal impacts associated with different societal choices.

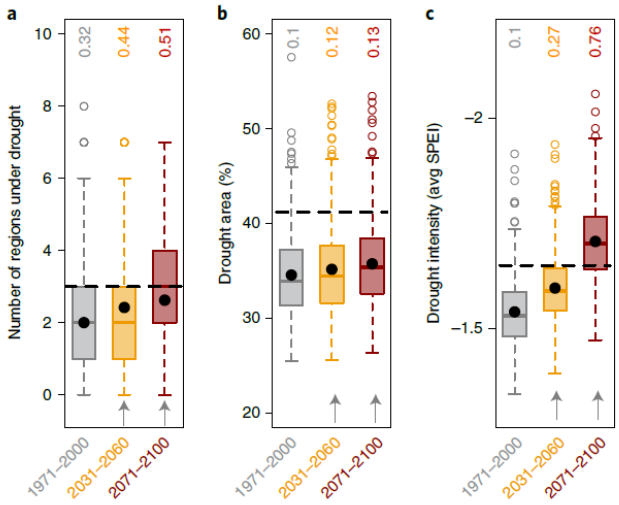

Fig. 1 | Historical and future characteristics of compound droughts in CESM. a, The distributions of the number of regions simultaneously under drought in historical (1971–2000) and future (2031–2060 and 2071–2100) climates. **b**-**c**, The distribution of drought area and intensity associated with compound droughts. Horizontal black dashed lines indicate the threshold used to define compound drought (that is, ≥3 regions under drought) in panel (**a**), widespread compound drought (that is, events with >90th percentile of total area (~41%) across all ten regions concurrently affected by drought) in panel (**b**) and severe compound drought (that is, the average SPEI across all drought-affected areas <10th percentile (less than ~−1.65)) in panel (**c**). The numbers above the boxplots indicate the probabilities of all (**a**), widespread (**b**) and severe (**c**) compound droughts. Grey arrows at the bottom of the panels indicate significant differences in the future distributions of drought regions, drought area and intensity relative to the historical climate at the 5% significance level. Black dots show the mean of the distribution in each boxplot.

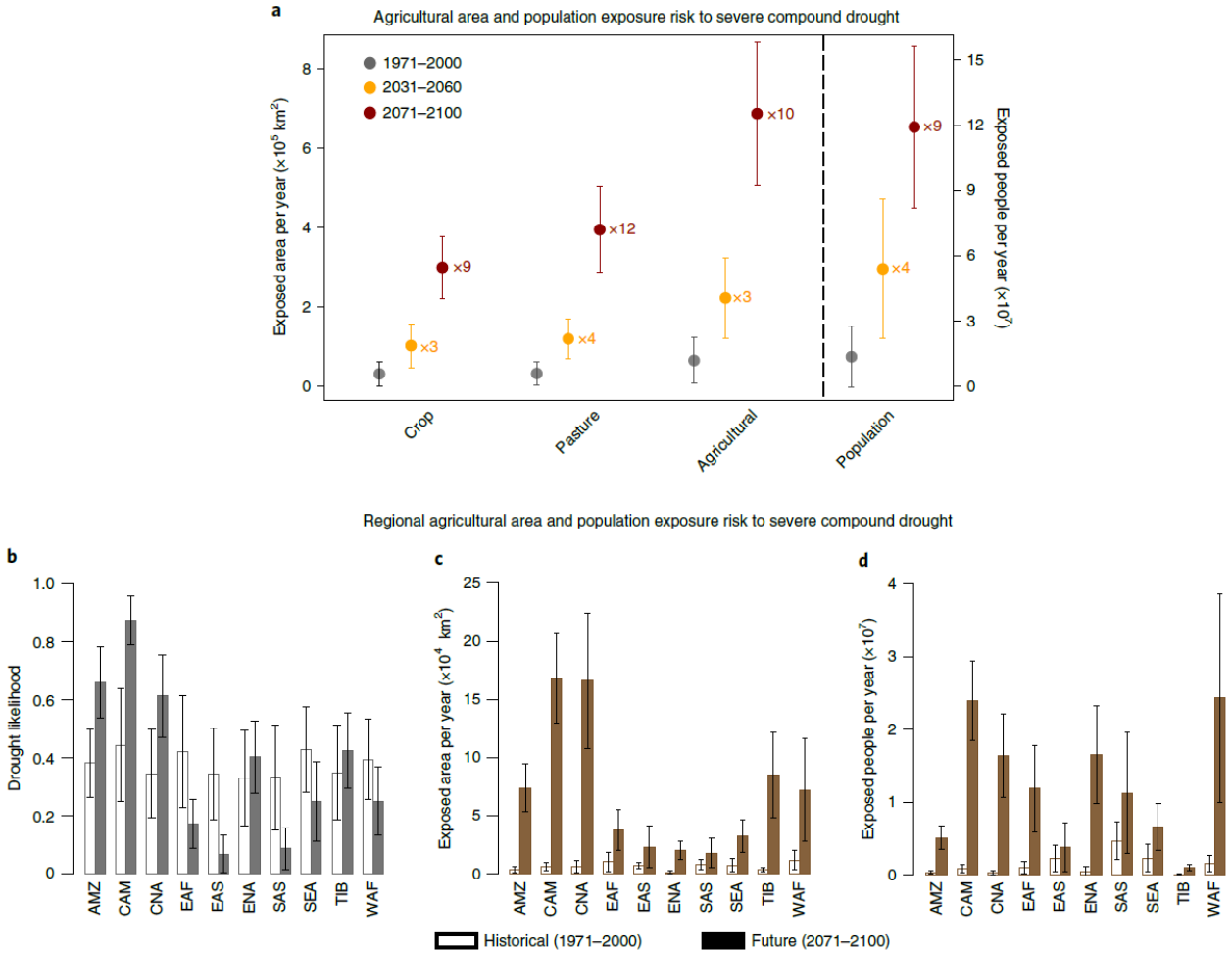

Fig. 2 | Crop, pasture lands and population exposure to severe compound droughts. a, Exposure of agricultural areas and population (changing under SSP5) to severe compound droughts in historical (1971–2000), mid-twenty-first century (2031–2060) and late twenty-first century (2071–2100) climates. Text beside the dots indicate the *N*-fold changes in exposure during future climates relative to historical. **b**, The fraction of instances in which a particular region is part of a severe compound drought event in historical and late twenty-first century. **c**,**d**, Regional average agricultural area (total cropland and pastureland) exposed (**c**) and number of people exposed to severe compound droughts (**d**) in historical and late twenty-first century climates. Error bars indicate uncertainties (ensemble spread of $\pm 1\sigma$) in the drought likelihood and exposures.

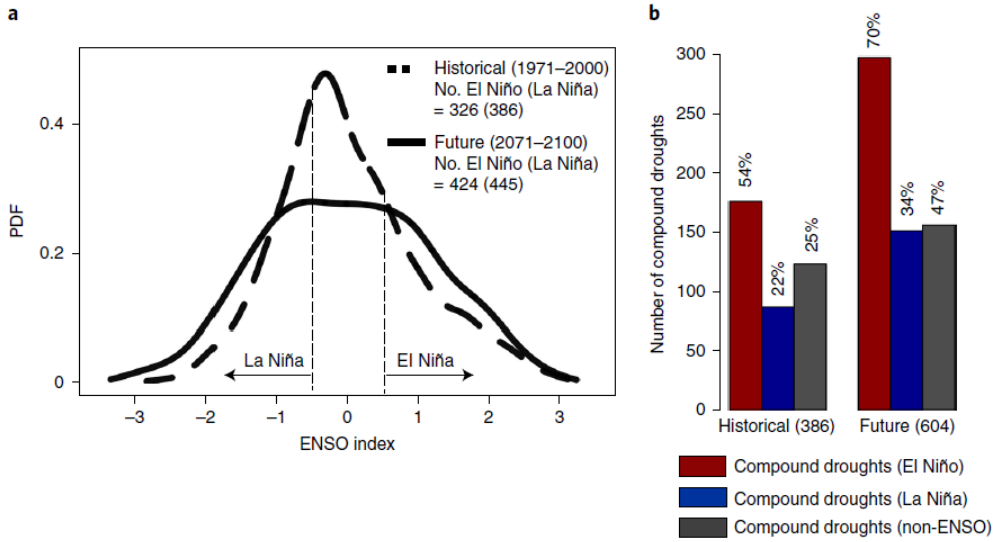

Fig. 3 | Projected changes in the frequency of ENSO events and compound droughts. a, The probability distribution function (PDF) of the ENSO index in the historical (1971–2000) and late twenty-first century (2071–2100) climate. The text indicates the number of El Niño (ENSO > 0.5σ) and La Niña (ENSO < −0.5σ) events across all 40 ensemble members in the 30-year climate periods (1,200 sample years). **b**, The count of compound droughts associated with El Niño events, La Niña events and non-ENSO drivers. The numbers on the *x*-axis indicate the total number of compound droughts in the historical and future climates; the percentages of El Niño events, La Niña events and non-ENSO events associated with compound droughts are shown above each bar .

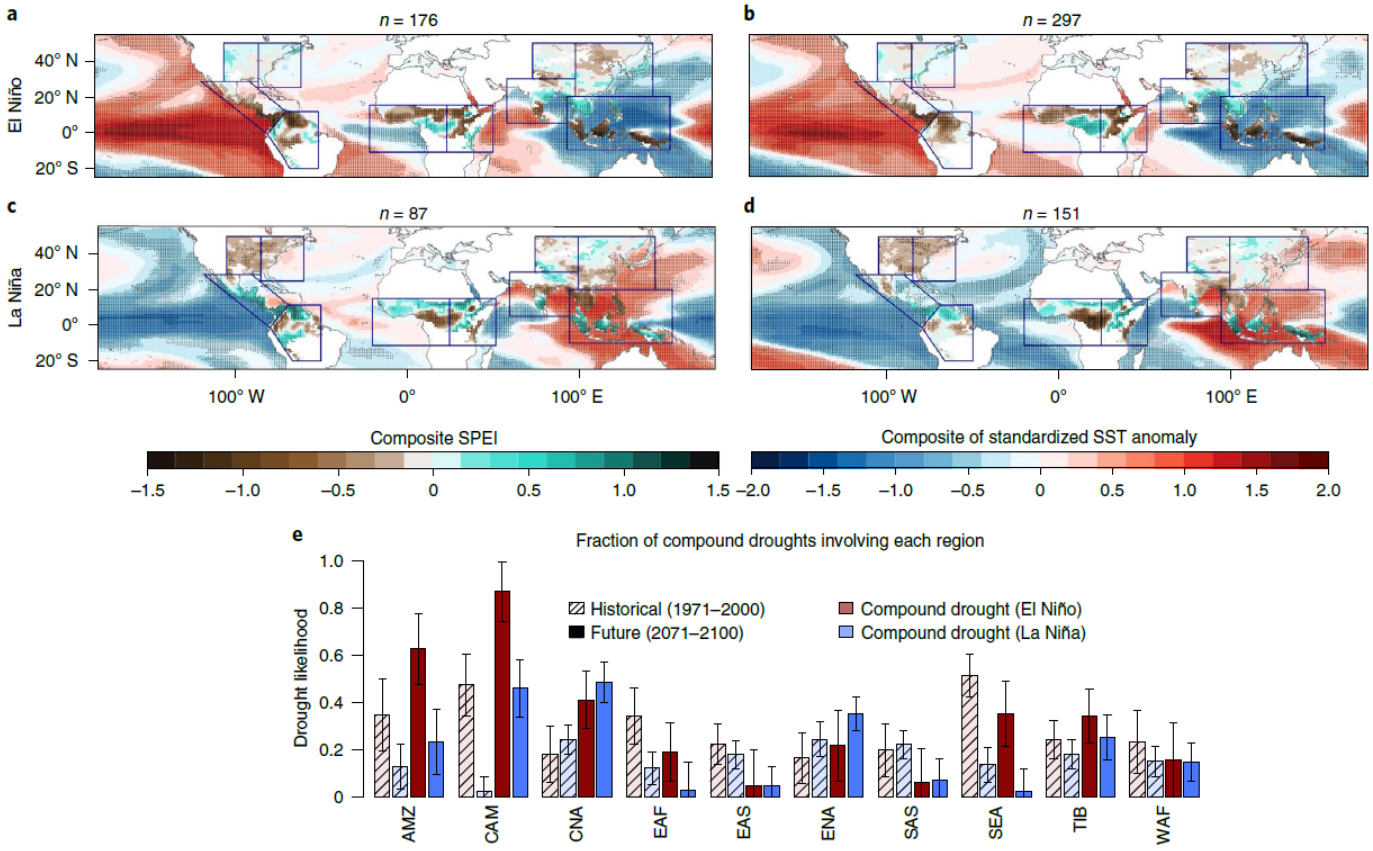

Fig. 4 | Simulated composites of detrended SPEI and detrended SST anomalies during compound droughts. a–**d**, The composite of standardized SST and SPEI anomalies during compound droughts associated with El Niño (**a**,**b**) and La Niña (**c**,**d**) events in the historical (1971–2000; **a**,**c**) and late twenty-first century (2071–2100; **b**,**d**) climates. Black dots over grid cells indicate consistency (>65% of sample years involved in the composite show same sign of SPEI) in the sign of SST anomalies and SPEI in the composites. Numbers (*n*) in the panel heading indicate the number of summer seasons with compound droughts used in each composite. **e**, Fraction of instances in which a particular region is part of a compound drought event associated with El Niño and La Niña events in each climate. Error bars indicate uncertainties (ensemble spread of ±1σ) in the drought likelihood.

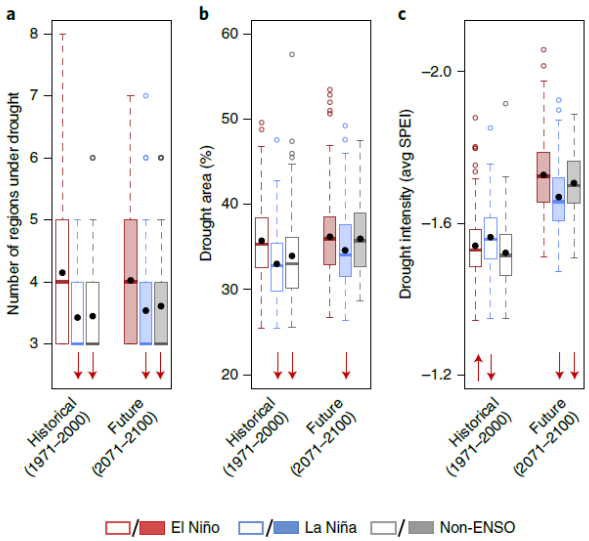

Fig. 5 | Influence of ENSO and non-ENSO drivers on compound drought characteristics. a–c, The distribution of number of regions simultaneously under drought (**a**), drought area (**b**) and drought intensity (**c**) associated with compound droughts during El Niño, La Niña and non-ENSO events in historical and late twenty-first century climates. Red downwards (upwards) arrows below the boxplots in each panel show significant negative (positive) differences in the mean drought characteristics associated with La Niña and non-ENSO relative to El Niño at the 5% significance level. Black dots show the mean of the distribution in each boxplot.

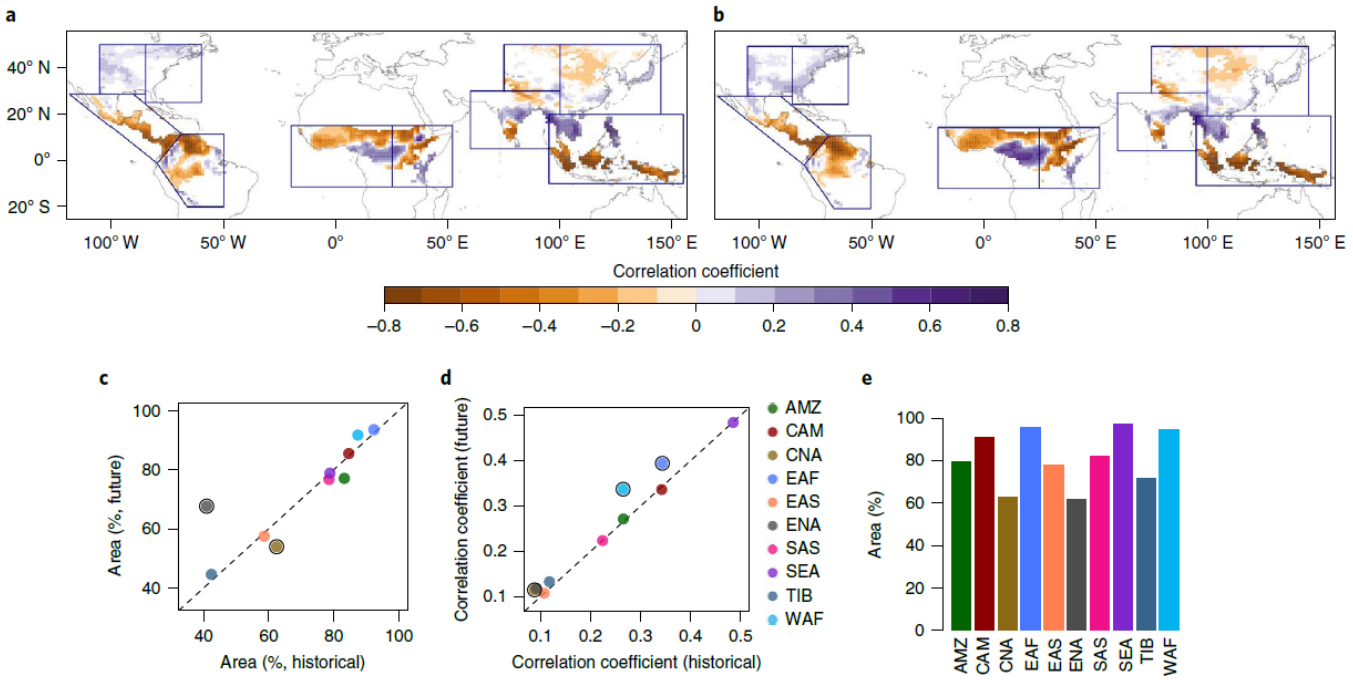

Fig. 6 | Changes in the ENSO teleconnections with SPEI over land in future climate. a,**b**, Correlation between ENSO and SPEI in the historical (1971–2000) (**a**) and late twenty-first century climate (2071–2100) (**b**). **c**, Area with significant (P-value < 0.05) correlation between ENSO and SPEI across all regions in the future relative to the historical climate. **d**, Strength of correlation (average absolute correlation coefficient) between ENSO and SPEI across all regions in the future relative to historical. The regions marked with black circles in **c** and **d** experience significant (P-value < 0.05) differences in the corresponding metric between the two climates. **e**, The fractional area in the historical climate that has similar sign of significant (P-value < 0.05) correlations in the future climate.

References

1. Zscheischler, J. et al. A typology of compound weather and climate events. Nat. Rev. Earth Environ. 1, 333–347 (2020).

2. AghaKouchak, A. et al. Climate extremes and compound hazards in a warming world. Annu. Rev. Earth Planet. Sci. 48, 519–548 (2020).

3. Zscheischler, J. et al. Future climate risk from compound events. Nat. Clim. Change 8, 469–477 (2018).

4. Leonard, M. et al. A compound event framework for understanding extreme. WIREs Clim. Change 5, 113–128 (2014).

5. Raymond, C. et al. Understanding and managing connected extreme events.

Nat. Clim. Change 10, 611–621 (2020).

6. Sarhadi, A., Ausín, M. C., Wiper, M. P., Touma, D. & Diffenbaugh, N. S. Multidimensional risk in a nonstationary climate: joint probability of increasingly severe warm and dry conditions. Sci. Adv. 4, aau3487 (2018).

7. Mishra, V., Thirumalai, K., Singh, D. & Aadhar, S. Future exacerbation of hot and dry summer monsoon extremes in India. npj Clim. Atmos. Sci. 3, 1–9 (2020).

8. Raveh-Rubin, S. & Wernli, H. Large-scale wind and precipitation extremes in the Mediterranean: a climatological analysis for 1979–2012. Q. J. R. Meteorol. Soc. 141, 2404–2417 (2015).

9. Kornhuber, K. et al. Amplified Rossby waves enhance risk of concurrent heatwaves in major breadbasket regions. Nat. Clim. Change 10, 48–53 (2020).

10. Heslin, A. et al. Simulating the cascading effects of an extreme agricultural production shock: global implications of a contemporary US dust bowl event. Front. Sustain. Food Syst. 4, 1–12 (2020).

11. Anderson, W., Seager, R., Baethgen, W. & Cane, M. Trans-Pacific ENSO teleconnections pose a correlated risk to agriculture. Agric. Meteorol. 262, 298–309 (2018).

12. Anderson, W. B., Seager, R., Baethgen, W., Cane, M. & You, L. Synchronous crop failures and climate-forced production variability. Sci. Adv. 5, 1–10 (2019).

13. Gaupp, F., Hall, J., Hochrainer-stigler, S. & Dadson, S. Changing risks of simultaneous global breadbasket failure. Nat. Clim. Change 10, 54–57 (2019).

14. Tigchelaar, M., Battisti, D. S., Naylor, R. L. & Ray, D. K. Future warming increases probability of globally synchronized maize production shocks. Proc. Natl Acad. Sci. USA 115, 6644–6649 (2018).

15. Singh, D. et al. Climate and the global famine of 1876–78. J. Clim. 31, 9445–9467 (2018).

16. Mehrabi, Z. & Ramankutty, N. Synchronized failure of global crop production. Nat. Ecol. Evol. 3, 780–786 (2019).

17. Mills, E. Insurance in a climate of change. Science 309, 1040–1044 (2005).

18. Levermann, A. Climate economics: make supply chains climate-smart. Nature

506, 27–29 (2014).

19. Singh, J., Moetasim, A., Skinner, C. B., Anderson, W. B. & Deepti, S. Amplified risk of

spatially compounding droughts during co-occurrences of modes of natural ocean variability. npj

Clim. Atmos. Sci. 4, 1–14 (2021).

20. Rogers, C. D. W. et al. Recent increases in exposure to extreme humid-heat events disproportionately affect populated regions. Geophys. Res. Lett. 48, 1–13 (2021).

21. Anderson, W. B., Seager, R., Baethgen, W., Cane, M. & You, L. Synchronous crop failures and climate-forced production variability. Sci. Adv. 5, 1–10 (2019).

22. IPCC Managing the Risks of Extreme Events and Disasters to Advance Climate Change Adaptation (eds Field, C. B. et al.) (Cambridge Univ. Press, 2012).

23. Kitoh, A. et al. Monsoons in a changing world: a regional perspective in a global context. J. Geophys. Res. Atmos. 118, 3053–3065 (2013).

24. Byers, E. et al. Global exposure and vulnerability to multi-sector development and climate change hotspots. Environ. Res. Lett. 13, 055012 (2018).

25. Han, T., Wang, H. & Sun, J. Strengthened relationship between eastern ENSO and summer precipitation over northeastern China. J. Clim. 30, 4497–4512 (2017).

26. Kumar, K. K., Rajagopalan, B. & Cane, M. A. On the weakening relationship between the Indian monsoon and ENSO. Science 284, 2156–2159 (1999).

27. Silvestri, G. E. El Niño signal variability in the precipitation over southeastern South America during austral summer. Geophys. Res. Lett. 31, 1–5 (2004).

28. Wang, B., Liu, J., Kim, H. J., Webster, P. J. & Yim, S. Y. Recent change of the global monsoon precipitation (1979–2008). Clim. Dyn. 39, 1123–1135 (2012).

29. Cook, B. I. et al. Twenty-first century drought projections in the CMIP6 scenarios. Earth's Future 8, 1–20 (2020).

30. Rowell, D. P., Booth, B. B. B., Nicholson, S. E. & Good, P. Reconciling past and future rainfall trends over East Africa. J. Clim. 28, 9768–9788 (2015).

31. Jones, B. & O'Neill, B. C. Spatially explicit global population scenarios consistent with the shared socioeconomic pathways. Environ. Res. Lett. 11, 084003 (2016).

32. Cai, W. et al. Increased frequency of extreme La Niña events under greenhouse warming. Nat. Clim. Change 5, 132–137 (2015).

33. Cai, W. et al. Increasing frequency of extreme El Niño events due to greenhouse warming. Nat. Clim. Change 4, 111–116 (2014).

34. Herrera-Estrada, J. E. et al. Reduced moisture transport linked to drought propagation across North America. Geophys. Res. Lett. 46, 5243–5253 (2019).

35. Miralles, D. G., Gentine, P., Seneviratne, S. I. & Teuling, A. J. Land– atmospheric feedbacks during droughts and heatwaves: state of the science and current challenges. Ann. NY Acad. Sci. 1436, 19–35 (2019).

36. Pascale, S. et al. Weakening of the North American monsoon with global warming. Nat. Clim. Change 7, 806–812 (2017).

37. Lee, J. Y. & Wang, B. Future change of global monsoon in the CMIP5. Clim. Dyn. 42, 101–119 (2014).

38. Wang, B., Jin, C. & Liu, J. Understanding future change of global monsoons projected by CMIP6 models. J. Clim. 33, 6471–6489 (2020).

39. Takahashi, H. G. et al. Response of the asian summer monsoon precipitation to global warming in a high-resolution global nonhydrostatic model. J. Clim. 33, 8147–8164 (2020).

40. Chiodi, A. M. & Harrison, D. E. Global seasonal precipitation anomalies robustly associated with El Niño and La Niña events—an OLR perspective. J. Clim. 28, 6133–6159 (2015).

41. Deser, C. et al. Insights from Earth system model initial-condition large ensembles and future prospects. Nat. Clim. Change 10, 277–286 (2020).

42. Fasullo, J. T., Otto-Bliesner, B. L. & Stevenson, S. ENSO's changing influence on temperature, precipitation, and wildfire in a warming climate. Geophys. Res. Lett. 45, 9216–9225 (2018).

43. Yun, K.-S. et al. Increasing ENSO–rainfall variability due to changes in future tropical temperature–rainfall relationship. Commun. Earth Environ. 2, 4–10 (2021).

44. Fredriksen, H. B., Berner, J., Subramanian, A. C. & Capotondi, A. How does El Niño–Southern Oscillation change under global warming—a first look at CMIP6. Geophys. Res. Lett. 47, GL090640 (2020).

45. Cai, W. et al. Changing El Niño–Southern Oscillation in a warming climate. Nat. Rev. Earth Environ. 2, 628–644 (2021).

46. Lengaigne, M. & Vecchi, G. A. Contrasting the termination of moderate and extreme El Niño events in coupled general circulation models. Clim. Dyn. 35, 299–313 (2010).

47. Detailed Trade Matrix. Food and Agriculture Organization of the United Nations (FAOSTAT, accessed 1 March 2021); http://www.fao.org/faostat/en/#data/

48. Dalin, C., Wada, Y., Kastner, T. & Puma, M. J. Groundwater depletion embedded in international food trade. Nature 543, 700–704 (2017).

49. D'Odorico, P. et al. Global virtual water trade and the hydrological cycle: patterns, drivers, and socio-environmental impacts. Environ. Res. Lett. 14, 053001 (2019).

50. Graham, N. T. et al. Future changes in the trading of virtual water. Nat. Commun. 11, 1–7 (2020).

51. Barnston, A. G., Tippett, M. K., L'Heureux, M. L., Li, S. & Dewitt, D. G. Skill predictions during 2002–11: Is our ncreasing? Bull. Am. Meteorol. Soc. 93, 631–651 (2012).

52. Kay, J. E. et al. The community earth system model (CESM) large ensemble project: a community resource for studying climate change in the presence of internal climate variability. Bull. Am. Meteorol. Soc. 96, 1333–1349 (2015).

53. Funk, C. et al. The climate hazards infrared precipitation with stations—a new environmental record for monitoring extremes. Sci. Data 2,

1–21 (2015).

54. Shannon, C. A mathematical theory of communication. Bell Syst. Tech. J. 27, 623–656 (1948).

55. Gao, J. Global 1-km Downscaled Population Base Year and Projection Grids Based on the Shared Socioeconomic Pathways, Revision 01 (NASA, 2020).

56. Ramankutty, N., Evan A. T., Monfreda, C. & Foley, J. A. Global Agricultural Croplands, 2000 (NASA, 2010).

57. Mishra, A. K., Özger, M. & Singh, V. P. An entropy-based investigation into the variability of precipitation. J. Hydrol. 370, 139–154 (2009).

58. Vicente-Serrano, S. M., Beguería, S. & López-Moreno, J. I. A multiscalar drought index sensitive to global warming: the standardized precipitation evapotranspiration index. J. Clim. 23, 1696–1718 (2010).

59. Beguería, S., Vicente-Serrano, S. M., Reig, F. & Latorre, B. Standardized precipitation evapotranspiration index (SPEI) revisited: Parameter fitting, evapotranspiration models, tools, datasets and drought monitoring. Int. J. Climatol. 34, 3001–3023 (2014).

60. Milly, P. C. D. & Dunne, K. A. Potential evapotranspiration and continental drying. Nat. Clim. Change 6, 946–949 (2016).

61. Yang, Y., Roderick, M. L., Zhang, S., McVicar, T. R. & Donohue, R. J. Hydrologic implications of vegetation response to elevated CO2 in climate projections. Nat. Clim. Change 9, 44–48 (2019).

62. Berg, A. & McColl, K. A. No projected global drylands expansion under greenhouse warming. Nat. Clim. Change 11, 331–337 (2021).

63. Kooperman, G. J. et al. Plant physiological responses to rising CO2 modify simulated daily runoff intensity with implications for global-scale flood risk assessment. Geophys. Res. Lett. 45, 12457–12466 (2018).

64. Mankin, J. S. et al. Influence of internal variability on population exposure to hydroclimatic changes. Environ. Res. Lett. 12, 044007 (2017).

65. McKee, B. T., Nolan, D. J. & John, K. The relationship of drought frequency and duration to time scales. In 8th Conference on Applied Climatology 179–184 (1993).

66. Mishra, A. K. & Singh, V. P. A review of drought concepts. J. Hydrol. 391, 202–216 (2010).

67. Batibeniz, F. et al. Doubling of U.S. population exposure to climate extremes by 2050. Earth's Future 8, 1–14 (2020).

68. O'Neill, B. C. et al. Achievements and needs for the climate change scenario framework. Nat. Clim. Change 10, 1074–1084 (2020).

69. Rayner, N. A. et al. Global analyses of sea surface temperature, sea ice, and night marine air temperature since the late nineteenth century. J. Geophys. Res. D https://doi.org/10.1029/2002JD002670 (2003).

70. Maher, N., Matei, D., Milinski, S. & Marotzke, J. ENSO change in climate projections: forced response or internal variability? Geophys. Res. Lett. 45, 11,390–11,398 (2018).

71. Good, P. I. Permutation Tests: A Practical Guide to Resampling Methods for Testing Hypotheses (Springer, 1994).

72. Singh, J. et al. Enhanced Risk of Concurrent Regional Droughts with Increased Variability and Warming (Zenodo, 2021); https://doi.org/10.5281/odo.5759291

Methods

Datasets

We primarily use the 40-member CESM1 LENS (~$1.3^0 \times 0.9^0$) to examine the historical (1971–2000; 1,200 sample years from 40 members × 30 years) compounding droughts and their projected changes in future (2031–2060 and 2071–2100) climate under the RCP8.5 scenario[52]. Each ensemble member of CESM–LENS differs only in its initial atmospheric conditions and has identical external forcing, thereby providing an opportunity to comprehensively investigate the influence of internal variability under different climate conditions and isolate the forced response. The larger sample of climate under different levels of forcing provided by LENS reduces the possibility of identifying spurious changes in the compound drought and ENSO characteristics due to internal variability. We focus on CESM as it demonstrates high skill in reproducing the observed global precipitation patterns over the study regions[19], ENSO characteristics (for example, intensity, frequency and related global teleconnections)[32,33,42], and shows a consistent response of extreme ENSO conditions to varying El Niño and La Niña definitions (Supplementary Table 1); however, we also use CanESM2 (~$2.8^0 \times 2.8^0$) LENS from SMILE[41] to examine the inter-model difference in historical compound drought characteristics and their projected changes. We could not consider other models from SMILE due to unavailability of the evapotranspiration variable required to estimate SPEI. In addition to CESM1 and CanESM2, CSIRO MK36 has the data required to estimate compound drought but we neglect it as it poorly reproduces the precipitation behavior during El Niño conditions[33] (Extended Data Fig. 5); however, we use all models from SMILE to characterize uncertainties in the ENSO response to historical forcing and projected warming. We use observed monthly precipitation data for 1981–2019 from the Climate Hazards Group Infrared Precipitation with Stations (CHIRPS) v.2 (ref. [53]) (~$0.25^0 \times 0.25^0$) to estimate the Shannon Entropy index[54], which is used to identify the regions of high variability in the summer precipitation. CHIRPS combines satellite-based precipitation estimates with in situ observations and models of terrain-based precipitation to provide spatially fine and continuous data[53]. For the calculation of changes in population and agricultural land exposures, historical (for the year 2000) and projected future population (for the year 2100) at 1 km spatial resolution[55] (https://sedac.ciesin.columbia.edu/data/set/popdynamics-1-km-downscaled-pop-base-year-projection-ssp-2000-2100-rev01), and crop and pastureland fraction (based on the year 2000) (https://sedac.ciesin.columbia.edu/data/set/aglands-pastures-2000) at 10 km spatial resolution[56] are obtained from the NASA Socioeconomic Data and Applications Center. We consider the population projections from the SSP5 to quantify the population exposure to compound droughts under projected future warnings.

Selection of Regions

Amazon (AMZ), Central America (CAM), Central North America (CNA), East Africa (EAF), East Asia (EAS), East North America (ENA), South Asia (SAS), Southeast Asia (SEA), Tibetan Plateau (TIB) and West Africa (WAF) (Extended Data Fig. 1a). We consider these regions because many of the regions: (1) receive the largest fraction of annual precipitation during the summer season (June– September; JJAS)[23,28] (Extended Data Fig. 1b) and exhibit strong variability in monthly summer precipitation, indicating the potential for droughts (Extended Data Fig. 1a,c); (2) are connected by similar physical processes, specifically the global boreal summer monsoon systems; (3) experience substantial precipitation variability associated with a major mode of climate variability, that is, ENSO[28] (Extended Data Fig. 1d); and (4) include several major breadbaskets and populations vulnerable to climate variability and change[24]. This approach follows the methodology used to identify and characterize historical compound drought characteristics in Singh and colleagues[19].

To identify the subregions that exhibit high variability in summer precipitation, we estimate the observed Shannon Entropy Index[54] using monthly summer precipitation from the CHIRPS dataset. We only consider those regions that show high variability (entropy > 4.86; median entropy values across the areas studied) in the monthly summer precipitation over at least 30% of their total area (Extended Data Fig. 1a). The Shannon Entropy H is estimated using equation (1)[57].

$$H = -\sum p_i \log_2 p_i \qquad (1)$$

where, p is the probability of each ith value of the time series.

Drought characteristics.

We use SPEI to define drought[58,59]; SPEI is estimated using a simple climatic water balance, that is, the difference between the accumulated summer season precipitation and evapotranspiration[58]. We use simulated evapotranspiration to calculate SPEI instead of estimates of potential evapotranspiration as, although potential evapotranspiration estimators such as Penman–Monteith account for the radiative influence of elevated atmospheric CO_2 on evapotranspiration[60–62], they do not account for changes in transpiration driven by plant physiological responses to elevated CO_2 (for example, those driven by changes in stomatal conductance). As stomatal conductance in the Community Land Model version 4 coupled within CESM1 is sensitive to atmospheric CO_2 concentration (as well as to photosynthesis and various climatic variables), the use of simulated evapotranspiration captures this key physiological control on future water balance[52,63]. We compute evapotranspiration as the sum of ground and canopy evaporation and transpiration for the present and future climates from CESM–LENS following the approach provided by Mankin et al.[64]. To construct SPEI, we follow a procedure similar to the calculations proposed by McKee et al. [65]. We use a log-logistic distribution to estimate the probability distribution of precipitation minus evapotranspiration (P-ET), instead of the Gamma distribution[58] that is used for SPI[66]. The gamma distribution requires a variable with non-negative values, which makes it inappropriate for SPEI estimation because the P-ET may yield negative values. Hence we estimate the probability of P-ET based on the widely used two-parameter log-logistic distribution and then transform it to a standard normal distribution to make it comparable across space and time[58,59]. Future (2031–2060 and 2071–2100) SPEI calculations use log-logistic distribution parameters fitted over the historical (1971–2000) climate to characterize changes in compound droughts relative to the historical climate.

Regional drought characteristics. We define an individual region as experiencing drought if its fractional area experiencing dry conditions (SPEI < −1) exceeds the eightieth percentile of the historical average drought area (1971–2000)[19].

Compound drought characteristics. A compound drought event is identified if at least three of the ten SREX regions concurrently experience drought. Compound drought area is defined as the fraction of the total area across the regions involved in compound droughts events. Similarly, the compound drought intensity is computed as the average SPEI over drought-affected areas across those regions. Widespread compound droughts are events with drought-affected areas exceeding the ninetieth percentile (~41% in CESM and ~37% in CanESM2) of the area of all historical compound droughts. Severe compound droughts are events with intensity lower (that is, more severe) than the 10th percentile (less than around −1.65 in CESM and –1.66 in CanESM2) of historical compound drought intensities. Other drought events with intensity above this threshold are referred to as moderate compound droughts and have a minimum intensity of −1. We use these thresholds to categorize compound drought into moderate and widespread events to quantify the influence of changes in drought area and intensity on agricultural and population exposure. The probability of compound drought is calculated as the ratio of the number of instances with compound drought to the total number of years in study period (40 members × 30 years = 1,200 sample years in CESM–LENS and 50 members × 30 years = 1,500 sample years in CanESM2 LENS). The probability of widespread and severe compound drought is estimated based on non-parametric Gaussian Kernel probability distribution.

Cropland, pastureland and population exposure.

There is a mismatch between the horizontal grid spacing of climate data and cropland, pastureland and population datasets. Moreover, the rate of population growth varies across space and depends on several local and global spatial interactions[31]. It is therefore not appropriate to use interpolation methods to upscale the population data to match ~1° CESM grid cells. Therefore, instead of remapping, we aggregate the population across the grid cells (at 1 km spatial resolution) that fall inside the ~1° CESM grid cells to calculate population exposure. We follow same procedure for crop and pasture lands. Given the importance of cropland for food cultivation and pastureland for animals grazing, we quantify the risk of exposure of these land droughts. The risk of cropland, pastureland and population exposures are calculated as follows:

$$\text{Cropland and pastureland exposure}: \frac{1}{N}\sum_{i=1}^{n} a_i \qquad (2)$$

where, N is number of years, i indicates years with compound droughts events, n is number of compound droughts, a indicates the total drought-affected cropland or pastureland across the regions involved in the compound droughts. Cropland and pasture fixed for both present and future climates.

$$\text{Population exposure}: \frac{1}{N}\sum_{i=1}^{n} p_i \qquad (3)$$

where p indicates the number of people experiencing drought across the regions involved in the compound droughts. We consider historical population based on year 2000 values and projected future population based on year 2100 under SSP5 because it is the only SSP consistent with the radiative pathway of RCP8.5 in CMIP5[31,67,68].

Large-scale modes of variability. We define the ENSO index using the average summer (JJAS) sea surface temperatures anomalies (SSTA) over the Niño3.4 region (5° S–5° N, 170° W–120° W)[69]. We remove the time-varying ensemble-mean SST from each member of the large ensemble, as follows:

$$\mathrm{SSTA}_{i,j} = \mathrm{SST}_{i,j} - \left(\frac{1}{40}\sum_{j=1}^{j=40}\mathrm{SST}_j\right)_i \qquad (4)$$

where i represents the year and j represents the ensemble member. After the mean SST warming signal is removed, we quantify ENSO characteristics in each ensemble member to sample the large internal variability in ENSO changes[70]. Differences in ENSO characteristics in individual ensemble members are probably dominated by natural variability. We therefore compare the distribution of ENSO characteristics based on all ensemble members in both climates to capture this internal variability. Given the size of the CESM large-ensemble, robust changes in characteristics between the distributions are indicative of forced changes in ENSO characteristics rather than changes due to internal variability. We then examine how these forced changes in ENSO affect compound drought characteristics under projected warming. By separating compound droughts associated with ENSO and non-ENSO drivers, our analysis aims to quantify the contribution of forced changes in ENSO to compound droughts.

El Niño and La Niña are defined as exceedances of $\pm 0.5\sigma$, where the standard deviation (σ) is estimated using the historical ENSO index values (1971–2000)[19]. We define an event as a non-ENSO event if the detrended Niño3.4 index is within $\pm 0.5\sigma$. Such events could be associated with occurrences of other modes of variability such as those identified in Singh et al.[19] as drivers of compound droughts such as the Indian Ocean Dipole, Atlantic Niño and Tropical North Atlantic or unrelated natural variability. Further to understand the ENSO response in various models and its sensitivity to varying definitions, we identify El Niño and La Niña events based on the definitions provided in Cai et al.[32,33] and Lengaigne and Vecchi[46]. Extreme El Niño events are defined if Niño3 JJAS rainfall exceeds 4 mm per day, whereas moderate El Niño events are defined if detrended Niño3 SST anomalies are $>0.5\sigma$ and they are not extreme El Niño events. Extreme La Niña events are defined when detrended Niño4 SST anomalies fall below -1.75σ, and moderate La Niña events are defined when detrended Niño4 SST anomalies fall below -0.5σ and they are not extreme La Niña events. We also highlight that JJAS precipitation over several of the regions studied shows the widespread and strongest correlation with contemporaneous ENSO[19], however, precipitation over a few regions is affected by ENSO at several month lag times since ENSO peaks during austral summer[46].

Statistical significance of the changes in compound droughts. We employ the non-parametric permutation test to assess the statistical significance of the differences in mean compound droughts characteristics in the historical and future climates[71]. We first quantify the test statistic (that is difference in the means of the distributions of compound droughts characteristics) from the two original historical and future distributions and then estimate an empirical distribution of the test statistic by randomly permuting the samples from the two distributions and re-estimating the test statistic from the resampled distributions, 10,000 times. If the original test statistic is higher (lower) than the 95th (5th) percentile of the empirical distribution, we consider the mean of compound droughts characteristics between historical and future climates to be significantly different at the 5% significance level. We also employ chi-square test to assess the statistical significance of differences in compound droughts associated with El Niño, La Niña and non-ENSO events.

Sensitivity of compound droughts changes. We use a bootstrap method to examine the sensitivity of compound drought changes to change in drought occurrence over a single region. We apply bootstrap resampling to every single region separately to randomize the drought occurrence over a particular region in each climate. Then, we estimate the number of drought regions in a particular year and estimate the probability of compound droughts in that particular bootstrapped drought distribution of number of regions simultaneously under drought. We repeat this procedure 1,000 times to obtain the distribution of compound drought probabilities.

Data Availability

All datasets used in the manuscript are publicly available. CESM1 LENS are publicly available through the Cheyenne cluster at /glade/collections/cdg/data/CLIVAR_LE. Observed CHIRPS precipitation data are publicly available at https:// www.chc.ucsb.edu/data/chirps. Population and agricultural land datasets are publicly available at NASA Data and Applications (https:// sedac.ciesin.columbia.edu).

Code Availability

The scripts developed to analyze these datasets are available from the corresponding author on reasonable request, and are also available in ref.[72].